# Optical properties of deep ice at the South Pole: absorption

The AMANDA Collaboration: Per Askebjer, Steven W. Barwick, Lars Bergström, Adam Bouchta, Staffan Carius, Eva Dalberg, Kevin Engel, Bengt Erlandsson, Ariel Goobar, Lori Gray, Allan Hallgren, Francis Halzen, Hans Heukenkamp, Per Olof Hulth, Stephan Hundertmark, John Jacobsen, Albrecht Karle, Vijaya Kandhadai, Igor Liubarsky, Doug Lowder, Tim Miller, Pat Mock, Robert M. Morse, Rodin Porrata, P. Buford Price, Austin Richards, Hector Rubinstein, Eric Schneider, Christian Spiering, Ole Streicher, Qin Sun, Thorsten Thon, Serap Tilav, Ralf Wischnewski, Christian Walck, and Gaurang B. Yodh

We discuss recent measurements of the wavelength-dependent absorption coefficients in deep South Pole ice. The method uses transit-time distributions of pulses from a variable-frequency laser sent between emitters and receivers embedded in the ice. At depths of 800–1000 m scattering is dominated by residual air bubbles, whereas absorption occurs both in ice itself and in insoluble impurities. The absorption coefficient increases approximately exponentially with wavelength in the measured interval 410–610 nm. At the shortest wavelength our value is approximately a factor 20 below previous values obtained for laboratory ice and lake ice; with increasing wavelength the discrepancy with previous measurements decreases. At ~415 to ~500 nm the experimental uncertainties are small enough for us to resolve an extrinsic contribution to absorption in ice: submicrometer dust particles contribute by an amount that increases with depth and corresponds well with the expected increase seen near the Last Glacial Maximum in Vostok and Dome C ice cores. The laser pulse method allows remote mapping of gross structure in dust concentration as a function of depth in glacial ice. 

## 1. Introduction

The AMANDA experiment (Antarctic Muon and Neutrino Detector Array) is a U.S.–Germany–Sweden collaboration with the aim of deploying a facility to detect neutrinos from astrophysical sources (a neutrino telescope) deep in the South Pole ice cap.[1] High-energy muon neutrinos will convert into charged muons through charged weak current interactions somewhere in the ice volume (or in the bedrock below the ice cap). As the muons are very penetrating, and move at relativistic speed, they will generate Cherenkov light along, typically, several hundred meters of track length. When the arrival times of Cherenkov photons are recorded at several locations in the ice volume, the direction of the muon track can be reconstructed. Interesting events will be muons coming from below the horizon, since they can only have been generated by upcoming neutrinos (all other known particles would be stopped in the interior of the Earth).

The AMANDA detector will eventually consist of many strings, each with 20–50 optical modules containing photomultiplier tubes (PMT's) lowered around 2 km into the ice. Typical spacing between strings and between modules in strings will be tens of meters.

P. Askebjer, L. Bergström, A. Bouchta, E. Dahlberg, B. Erlandsson, A. Goobar, P. O. Hulth, Q. Sun, and Ch. Walch are with Stockholm University, Sweden. S. W. Barwick, P. Mock, R. Porrata, E. Schneider, and G. Yodh are with the University of California, Irvine, California. S. Carius, A. Hallgren, and H. Rubinstein are with Uppsala University, Sweden. K. Engel, L. Gray, F. Halzen, J. Jacobson, V. Kandhadai, I. Liubarsky, R. Morse, and S. Tilav are with the University of Wisconsin, Madison, Wisconsin. H. Heukenkamp, S. Hundertmark, A. Karle, Ch. Spiering, O. Streicher, Th. Thon, and R. Wischnewski are with DESY Zeuthen, Germany. When this research was undertaken, D. Lowder, T. Miller, P. B. Price, and A. Richards were with the University of California, Berkeley, California. T. Miller is now with Bristol Research Institute, Delaware.

Received 8 July 1996; revised manuscript received 14 January 1997.

0003-6935/97/184168-13$10.00/0

The performance of the detector will depend crucially on the optical properties of the ice. A first stage of the detector, deployed during the 1993–1994 austral summer, consists of four vertical strings each having 20 PMT's spaced at 10-m distance. The strings form an 80-degree sector of a circle of 30.4-m radius, with one string at the center and three strings on the circumference. A laser calibration system was developed so as to determine the precise detector geometry and the optical properties of the ice. A brief summary of the results has been published recently.[2,3] The results have shown that the ice at 800–1000-m depth is highly turbid. The short scattering lengths (between 10 and 20 cm) are consistent with being due to a residual population of bubbles of trapped air. Deeper in the ice, these bubbles are expected to be transformed to air-hydrate crystals, which have a refractive index close to that of ice[4] and therefore should not cause much scattering. (For a thorough discussion of various scattering mechanisms in deep Antarctic ice, see companion paper.[5])

Surprisingly, the absorption coefficient of the ice at wavelengths between 400 and 600 nm was found to be smaller by a large factor (greater than 10 at the shortest wavelengths) than the value for laboratory ice[6,7] (for a compilation of several sets of experimental data see Ref. 8). The South Pole ice is thus a remarkably clear optical medium, and in the 1995–1996 season we deployed four new strings to a maximum depth of 2000 m, where air bubbles should have entirely transformed into air hydrates. The analysis of data from this deployment is in progress.

Because the reported AMANDA results (especially those of Ref. 3) deviate from previously published values by such a large factor, we believed that we should present to the optical physics community the details of our experimental method, the proposed explanation and implications of the long absorption lengths, and an analysis of absorption in dust present in the ice. Various sources of residual scattering at bubble-free depths are discussed in Ref. 5.

### 2. Outline of the Method to Extract Scattering and Absorption Lengths

The experimental setup for the measurement of the optical properties of the South Pole deep ice is shown in Fig. 1. Light from a dye laser (driven by a Nd:YAG laser) was brought down optical fibers to diffusing nylon spheres (one per PMT) approximately 30 cm below each PMT.

Pulsed laser light (4 ns FWHM) was fed into the optical fibers at a frequency of 10 Hz. By using gratings in the dye laser and a monochromator we could vary the wavelength of the light between 410 and 610 nm, with a precision of around 2 nm. (At shorter wavelengths, not enough light could be transmitted through the kilometer-long fibers.) After passage down the fiber, the 4-ns pulses had broadened to around 12 ns. Light was led down to one nylon sphere at a time, and the response of neighboring PMT's in the same string and in the other strings was recorded.

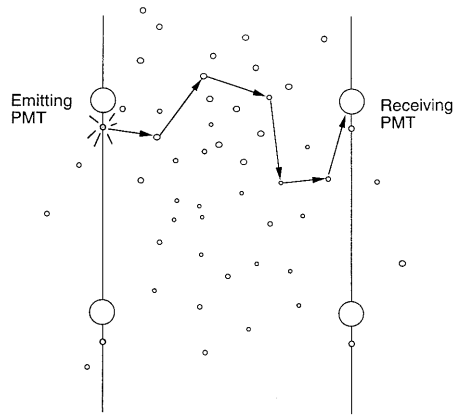


Fig. 1. Method for measuring scattering and absorption in deep ice: pulses at a desired wavelength are sent down one of 80 optical fibers to a diffusing sphere mounted immediately underneath a PMT module, and the distribution of arrival times is measured at one of the neighboring PMT's.

The PMT's [8-in. (20 cm) EMI 9353 tubes with a noise rate in the ice of approximately 1.7 kHz] were operated at a gain of $10^8$, and had approximately 6-ns resolution, including time smearing in the coaxial cables that fed the signals up to the surface. The signal from the PMT 30 cm from the flashing nylon sphere defined $t = 0$ (corrected for run time through fibers, etc.).

The main purpose of the laser system described above was to serve as a calibration system for the absolute timings of the PMT's and their relative positions in the AMANDA muon detector. Immediately after the system became operational it was realized, however, that the South Pole ice at depths between 800 and 1000 m is not an ideal optical medium for imaging the tracks of muons through their Cherenkov light. Instead of a narrow arrival pulse (expected typically at 87 ns for 20-m distance between emitting and receiving tube), a very broad structure with maximum at around 500 ns was observed (see Fig. 2). As exact timings are required to reconstruct the direction of muons from the sparsely sampled Cherenkov photons they generate, the observed timing pattern makes the present array not useful for muon tracking (but the array is used for other astrophysical applications[1]).

However, the presence of the broad time distributions, and our modeling of them, have permitted us to make more accurate measurements of the optical properties of ice in the visible region than have ever been done in the laboratory. As shown below, the *in situ* laser measurements in large volumes of ice and the random walk nature of the light propagation permit a clear separation between absorption and scattering, something that is extremely difficult to study in the laboratory.

In that process, we have independently discovered a method similar to one recently used in medical and other applications,[9] one difference being the longer time scales and distances involved here, another the fact that both the light emitters (nylon spheres) and

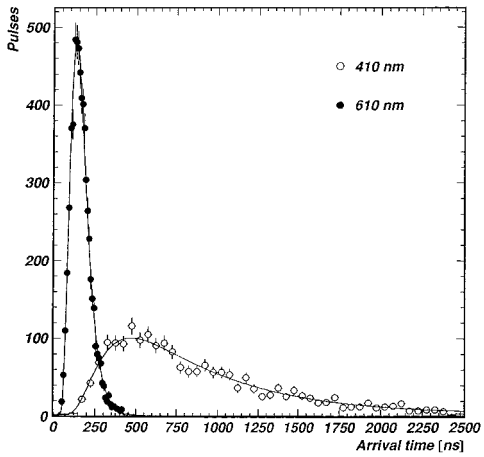


Fig. 2. Distribution of arrival times as measured and as fitted to the analytical formula Eq. (13) for an emitter and a receiver separated by 10 m. The results for wavelengths 410 and 610 nm are shown as open and filled circles, respectively. The fits shown give the same value for the scattering length $\lambda_{\text{bub}}$ (around 10 cm) for the two cases, but absorption lengths of around 230 and 10 m, respectively.

receivers (PMT tubes) are immersed in the medium to be measured. The derivation that we present of the relevant formulas seems to be new (and simple) and may be of interest for optical physics researchers. We also show that a detailed Monte-Carlo simulation of light propagation supports the analytical treatment and fits the measured distributions excellently.

### A. Random Walk Description of Light Propagation

The physical picture of photon propagation in the bubbly ice is that of a random walk. When a photon leaves the nylon sphere it passes through clear ice along a straight trajectory for some path length until it hits an air bubble. Then it is refracted (or externally reflected), traveling in a new direction until it hits the next bubble. The wide dispersion of arrival times at the PMT's must mean that a typical photon has undergone many scatterings, and therefore a probabilistic analysis of the random walk should be possible. The problem is simplified by the randomness of the medium and the macroscopic distances of propagation, which means that any interference effects can be ignored.

We define the simple, geometric scattering length on spherical bubbles as

$$\lambda_{\text{bub}} = \frac{1}{c_{\text{bub}}}, \tag{1}$$

with the scattering coefficient $c_{\text{bub}}$ given by

$$c_{\text{bub}} = \int_0^\infty \frac{dn_{\text{bub}}(r)}{dr}\,\pi r^2 dr, \tag{2}$$

where $dn_{\text{bub}}(r)/dr$ is the number density of bubbles having a radius between $r$ and $r + dr$ and $\pi r^2$ is the geometric cross section. This means that the probability distribution for the distance $d$ between two successive scatterings is proportional to $\exp(-d/\lambda_{\text{bub}})$. We note that the average geometric scattering length is

$$\langle d\rangle = \lambda_{\text{bub}}, \tag{3}$$

and the second moment is

$$\langle d^2\rangle = 2\lambda_{\text{bub}}{}^2. \tag{4}$$

We only have to incorporate two modifications to the standard random walk treatments given in the literature (e.g., Ref. 10), namely absorption of the light beam and the nonisotropy of the scattering amplitude for photons incident on air bubbles. Because the air bubbles themselves do not cause any absorption of photons, only scattering, it is simple to incorporate absorption in the random walk picture. Suppose that a photon arrives at a PMT after $N$ steps. Then the total path length is on the average $N\lambda_{\text{bub}}$, and absorption can be taken into account by weighting that particular path by the factor

$$\exp\left(\frac{-N\lambda_{\text{bub}}}{\lambda_a}\right). \tag{5}$$

(of course we assume $N \gg 1$; typically $N$ is of the order of 1000 in our problem), where $\lambda_a$ is the true absorption length (i.e., related to true absorption of photons in the medium).

Sometimes it is convenient to discuss absorption in terms of the absorption coefficient,

$$\alpha_{\text{abs}} = \frac{1}{\lambda_{\text{abs}}}. \tag{6}$$

This is related to the absorptive (imaginary) part of the index of refraction by

$$\alpha_{\text{abs}} = \frac{4\pi\,\text{Im}(n)}{\lambda_L}, \tag{7}$$

where $\lambda_L$ is the wavelength of the light source.

Nonisotropy of the scattering from bubbles means that there is a correlation between successive vectors making up the random walk. If the bubbles are spherical there is still an azimuthal symmetry, and one can show that (e.g., by introducing rotation matrices that rotate each successive vector to the polar axis),

$$\langle \mathbf{r}_1 \cdot \mathbf{r}_{1+k}\rangle = \lambda_{\text{bub}}{}^2(\delta_{0,k} + \tau^k), \tag{8}$$

where $\tau = \langle \cos\theta\rangle$ is the average of the cosine of the scattering angle, and the factor of 2 entering for $k = 0$ ($\delta_{0,k}$ is a Kronecker delta function) is a reflection of Eq. (3) and Eq. (4).

In the formula for random walk with absorption introduced as just explained,

$$W_N(\mathbf{R}) = \frac{1}{(2\pi\langle \mathbf{R}^2\rangle_N/3)^{3/2}}\exp\left(-\frac{3\mathbf{R}^2}{2\langle \mathbf{R}^2\rangle_N}\right)\exp\left(\frac{-N\lambda_{\text{bub}}}{\lambda_a}\right), \tag{9}$$

it just remains to evaluate

$$\langle \mathbf{R}^2 \rangle_N = \left\langle \left( \sum_{i=1}^{N} \mathbf{r}_i \right)^2 \right\rangle. \tag{10}$$

By expanding the squared sum in $\langle (\Sigma_{i=1}^{N} \mathbf{r}_i)^2 \rangle$, one finds $N$ terms with relative distance 0 (namely, $|\mathbf{r}_1|^2 + |\mathbf{r}_2|^2 + \ldots + |\mathbf{r}_N|^2$), $2(N-1)$ terms of relative distance 1 ($\mathbf{r}_1 \cdot \mathbf{r}_2 + \mathbf{r}_2 \cdot \mathbf{r}_1 + \ldots + \mathbf{r}_N \cdot \mathbf{r}_{N-1}$), and in general $2(N-k)$ terms of relative distance $k$.

Using Eq. (8), we find that the factor $2\lambda_{\text{bub}}{}^2$ can be taken outside and we arrive at

$$\begin{aligned} \langle \mathbf{R}^2 \rangle_N &= 2\lambda_{\text{bub}}{}^2 \sum_{k=0}^{N-1} (N-k)\tau^k \\ &= 2N\lambda_{\text{bub}}{}^2 \frac{(1-\tau) + (\tau^{N+1} - \tau)/N}{(1-\tau)^2}. \end{aligned} \tag{11}$$

In the limit of large $N$ we obtain

$$\langle \mathbf{R}^2 \rangle_N = \frac{2N\lambda_{\text{bub}}{}^2}{1-\tau}. \tag{12}$$

With the identification $N\lambda_{\text{bub}} = c_i t$, where $c_i = c/n$ is the velocity of light in the ice, we obtain the formula corresponding to the Green's function for the radiative transport of a spherically symmetric laser pulse emitted at a distance of $d = 0$ at time $t = 0$:

$$u(d, t) = \frac{1}{(4\pi D t)^{3/2}} \exp\left(\frac{-d^2}{4Dt}\right) \exp\left(\frac{-c_i t}{\lambda_a}\right), \tag{13}$$

with $d^2 = \mathbf{R}^2$, and where the constant of diffusion $D$ is given by

$$D = \frac{c_i \lambda_{\text{eff}}}{3}, \tag{14}$$

with the effective scattering length $\lambda_{\text{eff}}$ related to $\lambda_{\text{bub}}$ through the formula

$$\lambda_{\text{eff}} = \frac{\lambda_{\text{bub}}}{1-\tau}. \tag{15}$$

We note that in the expression for $D$ only the refractive scattering part of the optical amplitude needs to be taken into account. If diffraction or any other small-angle scattering effect is included, making the geometric bubble cross section increase from $\sigma$ to $(B+1)\sigma$, then

$$\lambda_{\text{bub}} \rightarrow \lambda_{\text{bub}}/(1+B), \tau \rightarrow (B+\tau)/(B+1),$$

and $D$ is easily seen to be invariant under these transformations. This has the simple physical interpretation that the diffusion power of the very forward-peaked diffraction has to be negligible compared with the large-angle scattering induced by refraction on bubble walls.

The formula (13) can be put in a more convenient form as follows, with two dimensionless quantities $y$ and $\kappa$. Defining $y = t/\sqrt{f}$ with

$$f = \frac{3\lambda_a d^2}{4c_i{}^2 \lambda_{\text{eff}}} \tag{16}$$

and the dimensionless quantity

$$\kappa = \frac{\sqrt{3}d}{2\sqrt{\lambda_a \lambda_{\text{eff}}}}, \tag{17}$$

one obtains

$$u(f, y) = \frac{C}{y^{3/2}} \exp[-\kappa(y + 1/y)], \tag{18}$$

with

$$C = \frac{1}{f^{1/4}(4\pi c_i \lambda_{\text{eff}}/3)^{3/2}}. \tag{19}$$

Using the basic integrals

$$\begin{aligned} &\int_0^\infty dy y^{-1/2} \exp(-\kappa(y + 1/y)] \\ &\quad = \int_0^\infty dy y^{-3/2} \exp[-\kappa(y + 1/y)] = \sqrt{\frac{\pi}{\kappa}} \exp(-2\kappa), \end{aligned} \tag{20}$$

one finds the average value of arrival time $t$ for a given distance $d$:

$$\langle t \rangle = \sqrt{f}\langle y \rangle = \sqrt{f} = \frac{\sqrt{3}d}{2c_i} \sqrt{\frac{\lambda_a}{\lambda_{\text{eff}}}}, \tag{21}$$

i.e., a linear relation.

In fact, defining the general class of integrals

$$f_I(\kappa, n) = \int_0^\infty dy y^{-(3/2)+n} \exp[-\kappa(y + 1/y)], \tag{22}$$

one finds a convenient recursion relation by taking the derivative of Eq. (22) with respect to $\kappa$:

$$f_I(\kappa, n+1) = -\frac{d}{d\kappa} f_I(\kappa, n) - f_I(\kappa, n-1), \tag{23}$$

with initial conditions for the recursion given by

$$f_I(\kappa, 0) = f_I(\kappa, 1) = \sqrt{\frac{\pi}{\kappa}} \exp(-2\kappa) \tag{24}$$

(the equality of $f_I(\kappa, 0)$ and $f_I(\kappa, 1)$, or more generally, $f_I(\kappa, n)$ and $f_I(\kappa, 1-n)$ is demonstrated easily when we let $y \rightarrow 1/y$ in the integral).

Using the arrival time distribution expressed in this scaling form, one can calculate easily all moments of the distribution, e.g., the expectation value

$$E(y) = 1, \tag{25}$$

and the variance

$$V(y) = E(y^2) - E(y)^2 = \frac{1}{2\kappa}. \quad (26)$$

The scaling form of the distribution was used in the numerical fitting procedure for the arrival times of the laser pulses.

The value of time $t_{\text{peak}}$ at which the distribution peaks is given by

$$t_{\text{peak}} = \frac{\sqrt{3}d}{2c_i}\sqrt{\frac{\lambda_a}{\lambda_{\text{eff}}}}\left(\sqrt{1 + \frac{3\lambda_a\lambda_{\text{eff}}}{4d^2}} - \frac{\sqrt{3\lambda_a\lambda_{\text{eff}}}}{2d}\right). \quad (27)$$

For the case at hand, with $\lambda_a \gg \lambda_{\text{eff}}$, this also gives an essentially linear dependence of $t_{\text{peak}}$ on $d$ (compared with $t_{\text{peak}} \propto d^2$ for a random walk process without attenuation).

### B. Application to Muons Traversing Bubbly Ice

The results for the Green's function derived here can also be used to obtain an expression for the time distribution of Cherenkov photons coming from a straight muon track, for which the closest approach (impact parameter) $d_i$ to the PMT at $t = 0$ is much larger than the scattering length $\lambda_{\text{eff}}$ (i.e., in our case greater than a meter or so). Introducing $a = 4\lambda_{\text{eff}}c_i/3$ and a cutoff length $l$ (the size of the detector), one finds

$$I(d_i, t; l) = N\sqrt{\frac{c_3}{c_1}}\int_{\max[0,\ \sqrt{c_3/c_1}(t-l/c_0)]}^{\sqrt{c_3/c_1}(t+l/c_0)} \frac{dz}{z^{3/2}} \times \exp\{-[\sqrt{c_1c_3}(z + 1/z) + c_2]\}, \quad (28)$$

where $N$ is a normalization factor, $c_0$ is the velocity of the muon (close to the velocity of light in vacuum), and

$$c_1 = ({d_i}^2 + {c_0}^2t^2)/a, \quad (29)$$

$$c_2 = -2{c_0}^2t/a, \quad (30)$$

$$c_3 = {c_0}^2/a + c_i/\lambda_a. \quad (31)$$

The total flux $F_\mu(d_i)$ received at a PMT of area $A_{\text{PMT}}$ from a muon generating $N_C$ photons per unit track length passing the PMT at impact parameter $d$ can be obtained (for $d_i \gg \lambda_{\text{bub}}$) when we integrate this expression over time and take the limit $l \to \infty$. We find

$$F_\mu(d_i) = \frac{3N_CA_{\text{PMT}}}{8\pi\lambda_{\text{eff}}}K_0\left(d_i\sqrt{\frac{3}{\lambda_{\text{eff}}\lambda_a}}\right), \quad (32)$$

where $K_0$ is a modified Bessel function of the second kind.

In applications where directional information and time structure at the submicrosecond level are not important, such as the detection of neutrinos from supernovae where relevant time scales are of the order of seconds, the present AMANDA detector in bubbly ice is perfectly functional. A neutrino-induced event from a supernova (SN) explosion typically generates a positron track of only 10 cm and can, on the diffusion scale $\sqrt{\lambda_a\lambda_{\text{eff}}}$, be regarded as pointlike. Then the total response function (flux per unit area integrated over time) for $N_{\text{SN}}$ photons (typically of the order of 3000 per positron) injected at distance $d$ is given by

$$I_{\text{SN}}(d) = \frac{3N_{\text{SN}}}{16\pi\lambda_{\text{eff}}d}\exp\left(-\sqrt{\frac{3}{\lambda_a\lambda_{\text{eff}}}}\,d\right). \quad (33)$$

We can define an effective volume of ice seen by a PMT by integrating $A_{\text{PMT}}$ times this flux over all space (the error caused by use of the formula at small $d$ where it is not strictly valid can be shown to be small, as it contributes a small fraction of the result). We then obtain

$$V_{\text{SN}} = \frac{N_{\text{SN}}A_{\text{PMT}}\lambda_a}{4}. \quad (34)$$

This result could (apart from the numerical factor) be anticipated on dimensional grounds with use of the observation that scatterings do not change the average photon flux (thus the result should not depend on the scattering length). For a real detector, correction factors related to the quantum efficiency of the PMT's and Poisson statistics of detected photons have to be added. Because the Cherenkov flux depends strongly on wavelength ($\sim 1/\lambda^2$) as do $\lambda_a$, the quantum efficiency and to some extent $\lambda_{\text{eff}}$, an integration over wavelength also has to be performed.

### C. Monte-Carlo Simulation of Light Propagation in Bubbly Ice

To verify that the general picture and derivations above are correct, we have also performed extensive Monte-Carlo simulations of light propagation through the ice. Thanks to the existence of widely separated length scales, $d \sim \lambda_a \gg \lambda_{\text{eff}} \gg \lambda_L$, where $\lambda_L$ is the wavelength of the laser light, a fairly simple optical treatment is adequate to obtain an estimate of $\lambda_a$ and $\lambda_{\text{eff}}$ good to a few percent accuracy or better. In fact, the estimate of $\lambda_a$ is given quite directly by the fall off of the arrival times of photons for large times and is insensitive to the uncertainties in the determination of $\lambda_{\text{bub}}$. To determine $\lambda_{\text{bub}}$ one needs the average value of the cosine of the scattering angle as input. One cause of uncertainty is that the bubbles may not be smooth enough to be regarded as perfect spheres. In that case, the diffusing ability could be greater (i.e., $\langle\cos\theta\rangle$ smaller) and $\lambda_{\text{bub}}$ consequently larger. Thus we are able to determine $\lambda_{\text{eff}}$ quite accurately from laser data, but the relation between $\lambda_{\text{eff}}$ and the geometric $\lambda_{\text{bub}}$ contains uncertainties. A direct measurement of the scattering function of air bubbles contained in the ice cores taken from the Antarctica would obviously be of importance for this problem.

Because photons from the coherent laser source scatter on the average between 500 and 1500 times on bubbles before arriving at the PMT's, the initial state in any single scattering can be regarded as being completely incoherent in phase, direction, and polarization. We have thus employed simple geometrical optics for the scattering process, incorporat-

ing singly refracted, externally reflected, and totally reflected light with the relative strength of the components given by the Fresnel coefficients. (In fact, we have also performed full Mie-scattering calculations and verified that the value of $\tau$ obtained from this simple analysis is correct.) We take into account the change of index of refraction of the air in the bubble that is due to the pressure and temperature. For the ice we use the wavelength-dependent values of the refraction index given in Ref. 11. The bubbles are assumed to be spherically symmetric, in agreement with observations at these depths.

Although a more complete treatment of the scattering could be implemented in the Monte Carlo, we emphasize that this, according to Eq. (15), only amounts to a renormalization of the relation between the effective scattering length $\lambda_{\text{eff}}$ and the geometric bubble scattering length $\lambda_{\text{bub}}$ (with the latter defined as an average over sizes and shapes of air inclusions), which is not important for discussion in this paper. (It is of importance, though, when discussing the implications of our results, e.g., for glaciology.) With our approximations we find for the quantity $\tau$ entering Eq. (15) a value around 0.75. This is slightly wavelength dependent as the refractive index of ice increases by some 2% when going from 600 to 300 nm. The Cherenkov angle $\arccos[1/(n_i\beta)]$ (where $\beta$ is the muon velocity in units of the speed of light in vacuum) will also increase by some 4% in going from the longest to the shortest wavelengths. (Because the intensity spectrum of the Cherenkov radiation varies as $1/\lambda^2$, the shorter wavelengths are most important for muon detection. Below 300 nm, however, the absorption in ice increases rapidly and the detection efficiency of the optical modules drops.)

### D. Fits to the Experimental Distributions

In making global fits to the laser calibration data, we used special routines that computed maximum likelihood fits to the observed distributions. The chi-squared method was used to give starting values for the maximum likelihood fit and to give a figure of merit of the fit. The Davidon variance metric algorithm[12] was used for the minimization, and the statistical errors were extracted from the variance matrix of the maximum likelihood procedure. The function used was formulated as

$$g(t) = \frac{x_n E_n \Delta x \exp(-T)}{y^{3/2}\mathcal{N}}, \tag{35}$$

where $x_n$ are the normalization constants for each measured arrival time distribution ($x_n \approx 1.0$), $E_n$ the number of events in distribution $n$, and $\Delta x$ the bin size used in all distributions,

$$T = \kappa\left(y + \frac{1}{y}\right),$$

$$y = \frac{t}{\sqrt{f}} \text{ or } \frac{t - \Delta t_m}{\sqrt{f}},$$

where $\Delta t_m$ allows for a shift in the definition of time zero for each emitting tube (this depends on details of the PMT such as the value of the high voltage, etc). We allowed for uncertainties in the vertical positions of the strings as this was difficult to determine during deployment. The initial chi-squared sum we minimized was

$$\chi^2 = \sum_{n=1}^{n_{\text{dis}}} \sum_{i=1}^{n_{\text{bins}}} \frac{[y_{i,n} - g(t)]^2}{y_{i,n}}, \tag{36}$$

where the $i$th bin in the $n$th distribution has a content of $y_{i,n}$ events and the theoretical prediction for this bin is $g(t)$.

There is a potential problem with this laser calibration method due to the fact that it is, in general, impossible to resolve several individual photons from the same laser pulse hitting the same PMT. Because the arrival time recorded by the receiving PMT is set by the first photon, one may tend to suppress long arrival times, which could underestimate the absorption length. To overcome this problem, we monitored the total number of emitted laser pulses $N$. For each receiving tube we then estimated the average number of photons reaching this detector from the zero class of a Poisson distribution. If the distribution has $n$ entries, the Poisson parameter $\mu$ is given by

$$P(0) = \exp(-\mu) = \frac{N - n}{N}, \tag{37}$$

i.e.,

$$\mu = \ln\left(\frac{N}{N - n}\right). \tag{38}$$

The variable used to select nonsaturated data is the sum of the zero class and the class with one photon,

$$\begin{aligned} \alpha &= P(0) + P(1) \\ &= \exp(-\mu) + \mu \exp(-\mu) \\ &= \exp(-\mu)(1 + \mu), \end{aligned} \tag{39}$$

i.e., $1 - \alpha$ is the fraction of events expected to have two or more photons reaching the detector and thus causing saturation. To avoid the saturation problem, we demanded that $1 - \alpha$ was less than 1%. To get a statistically significant estimate of the optical parameters, only time distributions where at least 2000 hits were registered by the receiving PM were selected. This left almost 500 time distributions for various wavelength and distance combinations.

In Fig. 2 we show the distribution of arrival times as measured and as fitted to the analytical expression [Eq. (13)] for our random walk model, for an emitter and a receiver separated by 10 m. The results for wavelengths 410 and 610 nm are shown as open and filled circles, respectively. The fits shown give the same value for the scattering length $\lambda_{\text{bub}}$ (around 10 cm) for the two cases, but absorption lengths of around 230 and 10 m, respectively. The quality of the analytical fit to the data is quite remarkable.

Table 1. Absorption Lengths $\lambda_{abs}$[a]

| Wavelength (nm) | $\lambda_{abs}^{830}$ (m) | $\lambda_{abs}^{970}$ (m) |
|---|---|---|
| 410 | 219.9 ± 12.5 | — |
| 415 | 225.6 ± 6.2 | 168.7 ± 23.6 |
| 420 | 227.4 ± 4.0 | 163.9 ± 7.1 |
| 435 | 207.4 ± 1.5 | 166.3 ± 1.9 |
| 450 | 171.3 ± 1.3 | 146.0 ± 2.1 |
| 475 | 117.1 ± 0.7 | 104.6 ± 1.2 |
| 500 | 68.9 ± 1.3 | 64.1 ± 1.0 |
| 530 | 38.3 ± 1.0 | 39.5 ± 0.7 |
| 590 | 12.0 ± 0.1 | 10.5 ± 0.3 |
| 610 | 10.3 ± 0.3 | — |

[a]The absorption lengths [i.e., the inverse of the absorption coefficients $\alpha_{abs}$ defined in Eq. (6)] for several laser wavelengths at two different depths, around 830 and 970 m, determined by the AMANDA calibration system in the South Pole ice. For 410 and 610 nm, only data for 830 m could be obtained.

We thus conclude that the physics behind the laser calibration data is well understood, and that we have, in fact, at our disposal a powerful tool to make *in situ* measurements of important properties of the ice such as $\lambda_a$ and $\lambda_{bub}$. In particular, $\lambda_a$ and $\lambda_{eff}$ are essentially uniquely determined by the temporal distribution of arrived photons at each particular PMT, once the geometry of the detector array is fixed.

We note that the values of $\lambda_a$ and $\lambda_{eff}$ obtained through this analysis are essentially spatial averages over the diffusion scale $(\lambda_a\lambda_{eff})^{1/2}$. Since we let these parameters depend on depth in the analysis, we are using an adiabatic approximation that should be excellent if the quantities vary slowly with depth. The goodness of the fit to the function (13) for all wavelengths and all depths shows the self-consistency of this scheme.

### 3. Summary of Experimental Results

In this section, we briefly summarize the results on absorption length as a function of wavelength obtained by the AMANDA calibration system at two depths, around 830-m and 970-m depth, respectively. In Ref. 3 results are also given for an intermediate region around 910 m, with results similar to those at the shallowest depth. The results are shown in Table 1 (for details, see Ref. 3). The errors given are only statistical; a systematic error estimated to be around 5% (dominated mainly by the uncertainty of the exact geometry of the AMANDA array should be added).

### 4. Modeling the Optical Properties of Highly Pure South Pole Ice

Using the results presented in Section 3, we next analyze the intrinsic optical properties of the South Pole ice and estimate the absorption that is due to solid impurities present in the ice. In the discussion we compare our results for South Pole ice with measurements made on less pure ice,[6–8] on extremely pure water,[13] and on LiF[14] as an example of a highly transparent solid.

#### A. Intrinsic Absorption in Highly Pure Ice

Our discussion is based on features shown in Figs. 3 to 5. We focus attention on three regions of the approximately V-shaped spectra with their minima in the visible region. On the ultraviolet side, the absorption in both ice[6–8] and ionic crystals[14] decreases exponentially at wavelengths somewhat longer than that corresponding to the electronic band-gap energy (~8 eV for ice, ~13 eV for LiF). The slope of this so-called Urbach tail is believed to be governed by exciton–phonon interactions; for LiF it becomes more shallow with increasing temperature.[14]

On the long wavelength side of the minimum, absorption rises approximately exponentially as a function of wavelength, but the window of transparency is much narrower for ice than for ionic crystals. Ionic crystals are transparent throughout the entire visible region, and their exponential absorption spectrum in the infrared is the result of multiphonon processes, in which a photon is absorbed with the emission of $n$ phonons. Phenomenological models[15] lead naturally to an exponential dependence of the absorption coefficient on wavelength, in agreement with measurement over 6 orders of magnitude, for $n$ up to at least seven phonons. The argument in the case of ionic crystals is that the contributions of overtones are generated by processes that depend on some coupling constant, with the $n$th overtone going as (coupling constant)$^{n-1}$. This leads naturally to an exponential dependence on overtone number.

In contrast, ice is a molecular crystal in which the $H_2O$ molecules are connected by weak OH—O hydrogen bonds. Each O atom in the lattice is coordinated to four H atoms, forming strong intramolecular bonds with two of them and hydrogen bonds with the other two. Ice absorbs much more strongly than do ionic crystals in the red region of the visible because ice has additional degrees of freedom associated with the stretching and bending of H—O—H bonds in individual water molecules. These internal modes lead to absorption in the red region. The fundamental stretching mode peaks at ~3 μm. Numerous overtones and combinations of stretching and bending modes with each other and with the lattice modes lead to a roughly exponential slope from a minimum at approximately 400 nm to a large peak at 3 μm. The extension of this exponential to values of the absorption coefficient below $10^{-1}$ m$^{-1}$ can be seen only if the ice is very pure and if the measurement technique is able to discriminate absorption against scattering.

By application of the same reasoning that applies to multiphonon absorption, we suggest that intramolecular vibrations depend on a coupling constant and that the overtones decrease as increasing powers of the coupling constant, thus leading to an exponential dependence of absorption on wavelength in the red and infrared. Because this conjecture assumes no growth in the number of processes with overtone number, the actual rate of increase of absorption with wavelength may, for large overtone numbers, be less rapid than exponential. (We make use of this assumption of an

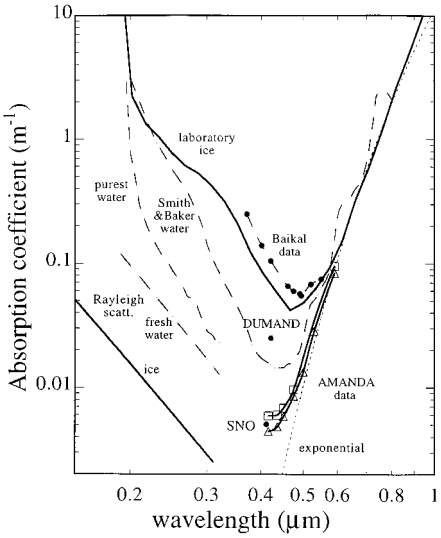


Fig. 3. Comparison of absorption spectra in the wavelength interval ~200 to ~800 nm for ice (solid curves and open symbols) and water (dashed curves and solid circles).

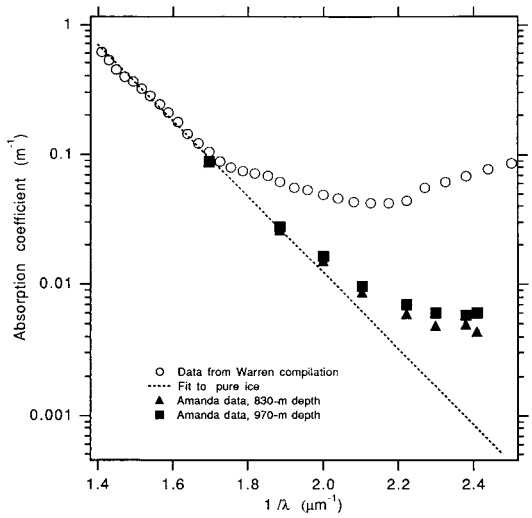


Fig. 4. Absorption as a function of wave number in μm$^{-1}$ for laboratory-grown ice crystals (open circles) and for South Pole ice at level 3 (830 m; filled triangular symbols) and level 17 (level 970 m; filled square symbols). The dotted curve is an exponential fit to data for laboratory ice at 600–800 nm.

exponential absorption in Subsection 4.B when we estimate the contribution of dust to absorption.)

Impurities, dislocations, vacancies, and their associated electronic defects contribute to absorption and scattering. Almost no measurement techniques, with the exception of our pulsed laser technique, are designed to be able to distinguish scattering from absorption. These defects tend to fill in the minimum in the spectrum to a degree that depends on their concentration and size distribution.

Figure 3 compares absorption data and the calculated magnitude of Rayleigh scattering for ice (solid curves and open symbols) and water (dashed curves and solid circles) at wavelengths near the absorption minimum. The most striking feature of the data is the large discrepancy between values of the absorption near the minimum. For water, the absorption decreases, in order, from the water of Lake Baikal,[16] to the Pacific Ocean (the DUMAND point),[17] to pure seawater (with no particulate content) as summarized by Smith and Baker,[18] to the curve labeled purest water, which gives the results of Quickenden and Irvin,[13] who took extraordinary measures to eliminate both inorganic and organic impurities, and finally to the point labeled SNO (Sudbury Neutrino Observatory). The SNO result is a recent measurement by Noël and Mes,[19] who went to great lengths to purify the water to be used in the SNO experiment.

The Lake Baikal group has recently used a pulsed laser at 475 nm to measure scattering separately from absorption. They find values of $\lambda_{scat} \approx 8 - 23$ m$^{-1}$, with $\langle \cos \theta \rangle \sim 17°$.[20] None of the authors of the other studies on water made a case for having been able to distinguish Rayleigh scattering from absorption. In fact, the data for purest water approach asymptotically (to within a factor 2) the calculated Rayleigh-scattering line for pure water.

The measurements in Fig. 3 labeled laboratory ice represent the contributions of a number of researchers,[6,7] none of whom took steps to measure scattering. In contrast, the AMANDA experiment measured both the scattered and the absorbed components separately for ice that is probably the purest, naturally occurring solid material on Earth. (The concentration of impurities in South Pole ice is discussed in Ref. 21.) At the minimum in the curve for laboratory ice, the absorption measured by AMANDA is approximately an order of magnitude lower than the Grenfell and Perovich[6] data. Figure 4 shows the region in more detail, with $\lambda^{-1}$ as the abscissa on a linear scale so that the exponential dependence can be more clearly noted.

The reader may have noticed that, in the interval ~0.2 to ~0.45 μm, the data for laboratory ice in Fig. 3 have a slope approximating the Rayleigh $\lambda^{-4}$ law, but approximately 2 orders of magnitude higher than the calculated contribution of Rayleigh (or thermal) scattering for pure ice indicated by the solid straight line. In Subsection 4.B and in Ref. 5 we suggest that the apparent absorption of laboratory ice in this interval may be due to Rayleigh scattering from defects in laboratory ice. The dotted curves in Figs. 3 and 4 are exponential fits to the data of Grenfell and Perovich[6] in the interval 0.6–0.8 μm. It represents our conjecture as to the intrinsic absorption of ice in the red region in the absence of impurities.

Figure 5 compares the absorption in ice and a number of transparent solids over a broad range of wavelengths. We draw attention to the lines representing fourth-power laws, $\lambda^{-4}$, that suggest scattering from crystalline defects with dimensions much smaller than the wavelength. The techniques used to obtain these data could not have distinguished scattering from absorption. Thus it is tempting to conclude that the portions of the absorption curves that exhibit the $\lambda^{-4}$ dependence are due mainly to

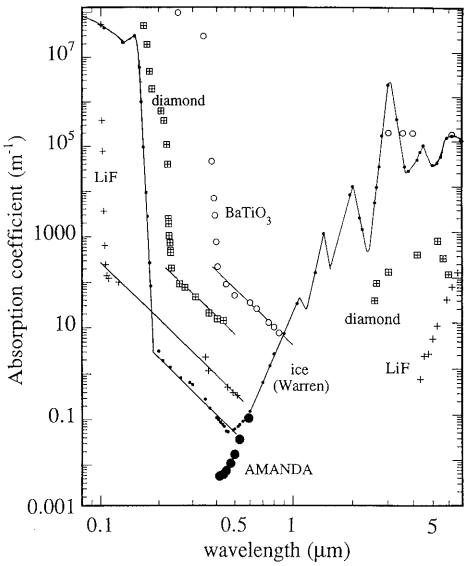


Fig. 5. Comparison of absorption spectrum in ice and a number of other transparent solids. The straight lines representing an inverse fourth-power law, $\lambda^{-4}$, are meant to show those portions of each spectrum that are due to Rayleigh scattering.

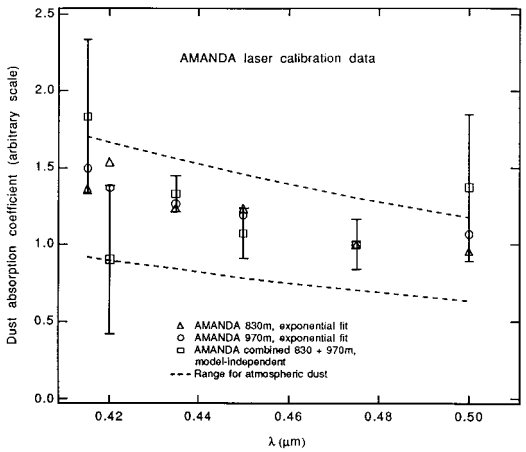


Fig. 6. Wavelength dependence of the absorption on dust inferred from the AMANDA laser measurements. The normalization is arbitrarily set to unity at $\lambda = 475$ nm. Open squares, and the error bars, refer to the model-independent analysis where the intrinsic absorption in ice has been subtracted. Open triangles and circles are values from AMANDA depths 830 and 970 m, respectively, with an exponential fit to the intrinsic ice absorption. The band within the dashed curves corresponds to the wavelength dependence measured for atmospheric dust at a U.S. location.[24]

impurity scattering instead of being due to absorption. In Ref. 5 we estimate the concentration, size, and type of defects necessary to account for the $\lambda^{-4}$ fits to the data.

### B. Absorption by Solid Dust Particles in Ice

We now focus on the AMANDA absorption data[3] taken at depths of 830 m (shown in Figs. 3 and 4 as triangular symbols) and at 970 m (shown in Figs. 3 and 4 as square symbols). Additional data, taken at a depth of 910 m, were indistinguishable from those taken at 830 m. The data[3] show convincingly that the absorption deviates more from the exponential extrapolation at 970 m than at 830 and 910 m. Our interpretation is that, in addition to the intrinsic absorption by perfect ice, dust particles with a greater concentration at 970 than at 830 and 910 m absorb light with a coefficient that decreases with increas ing wavelength. This interpretation is supported strongly by our model of age versus depth of South Pole ice, by means of which we predicted dust concentration to increase to a maximum at a depth slightly greater than 1000 m (Ref. 22).

We now derive the absorption coefficient as a function of wavelength for dust in South Pole ice, and we determine the ratio of dust concentration at 830 m to that at 970 m. When trying to extract absolute values for the contribution of solid impurities to the absorption coefficient, one encounters the problem of estimating the uncertainty involved in the exponential extrapolation of the intrinsic absorption coefficient of ice shown as the dotted curves in Figs. 3 and 4. We developed the following way to determine the wavelength dependence of the absorption of solid impurities, normalized to some particular wavelength, independent of the unknown intrinsic ice absorption. We write the measured absorption coefficient $\alpha_{\text{expt}}(h, \lambda)$ as

$$\alpha_{\text{expt}}(h, \lambda) = \alpha_{\text{int}}(\lambda) + \alpha_{\text{dust}}(h, \lambda) = \alpha_{\text{int}}(\lambda) + c_{\text{dust}}(h)\sigma_{\text{dust}}(\lambda), \quad (40)$$

which exploits the facts that the intrinsic ice absorption coefficient $\alpha_{\text{int}}(\lambda)$ and the absorption cross section of solid impurities $\sigma_{\text{dust}}(\lambda)$ are independent of depth, and the concentration of impurities $c_{\text{dust}}(h)$ is independent of wavelength. This assumes that the nature of solid impurities is independent of depth and only the concentration changes.[23]

By using Eq. (40) for two different wavelengths and two different depths, we can eliminate the unknowns $\alpha_{\text{int}}$ and $c_{\text{dust}}(h)$ and express the ratio of the absorption cross section at two wavelengths in terms of only experimentally measured quantities. The result is

$$\frac{\sigma_{\text{dust}}(\lambda_1)}{\sigma_{\text{dust}}(\lambda_2)} = \frac{\alpha_{\text{expt}}(h_1, \lambda_1) - \alpha_{\text{expt}}(h_2, \lambda_1)}{\alpha_{\text{expt}}(h_1, \lambda_2) - \alpha_{\text{expt}}(h_2, \lambda_2)}. \quad (41)$$

We will use for the analysis only the data for the six wavelengths that give the smallest statistical error. For $h_1$ we use data from phototubes at 830 m (around AMANDA level 3) and for $h_2$ we use data at 970 m (around AMANDA level 17). We normalize all impurity absorption cross sections to $\sigma_{\text{dust}}$ (475 nm), which has the most statistics of all the distributions. Figure 6 shows the result of this analysis. To test the natural hypothesis that the absorbing impurity is atmospheric dust that accumulated in the ice by precipitation onto the surface at the time the ice formed from snow,[23] we compared our results with measurements of the absorption spectra of various samples of atmospheric dust at U.S. locations.[24] As can be seen, our results are consistent with the hypothesis

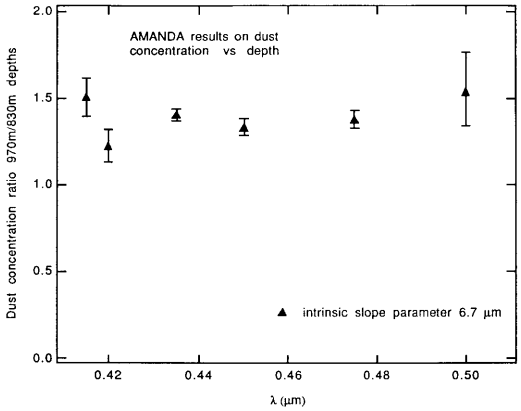


Fig. 7. Ratio of dust concentration at 970 and 830 m as obtained by our analysis in this paper. Note that the ratio does not depend on wavelength, which is a consistency check of the scheme employed.

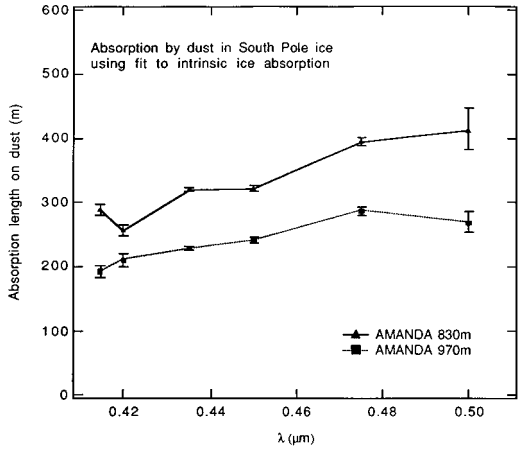


Fig. 8. The absorption length (i.e., the inverse of the absorption coefficient) given by scattering on impurities in the ice, as a function of wavelength for AMANDA 830-m level (filled triangles) and 970 m (filled squares). We obtained the values by subtracting the best-fit exponential for the intrinsic absorption from the measured absorption.

that we do observe absorption by dust. However, it must be noted that the model-independent analysis does not have small enough error bars to exclude, for example, a constant absorption coefficient.

In Fig. 6 we also included estimates based on the assumption that the intrinsic absorption spectrum of dust-free ice follows the exponential shown by a dotted curve in Fig. 4. The good fit shown in that figure was obtained by the expression

$$\alpha_{\mathrm{int}}(\lambda) = 81 \exp(-\lambda_0/\lambda)\ \mathrm{cm}^{-1}, \tag{42}$$

with the value $\lambda_0 \sim 6.7\ \mu\mathrm{m}$ being determined not only by a fit to the measured absorption in the near IR, but also requiring self-consistency of the *Ansatz* in Eq. (40). That is, the values obtained for dust concentration $c_{\mathrm{dust}}(h)$ with use of the experimental values $\alpha_{\mathrm{expt}}(h, \lambda)$ and the fitted $\alpha_{\mathrm{int}}(\lambda)$ should not depend on $\lambda$; neither should the derived $\sigma_{\mathrm{dust}}(\lambda)$ depend on $h$.

Using Eq. (40), we can derive the following expression for the ratio of the dust concentration at the lower level of the detector to the upper level:

$$\frac{c_{\mathrm{dust}}(970\ \mathrm{m})}{c_{\mathrm{dust}}(830\ \mathrm{m})} = \frac{\alpha_{\mathrm{expt}}(970, \lambda_1) - \alpha_{\mathrm{int}}(\lambda_1)}{\alpha_{\mathrm{expt}}(830, \lambda_1) - \alpha_{\mathrm{int}}(\lambda_1)}. \tag{43}$$

We can see in Fig. 7 that all wavelengths give the consistent result ~1.4 for this ratio.

Subtracting now the fitted intrinsic absorption coefficient from the measured one at each wavelength, we finally obtain values for the absorption length (i.e., the inverse of the absorption coefficient) that is due to dust at the two AMANDA levels. We find that the absorption length that is due to dust increases with wavelength and decreases with depth, with typical values being 200–300 m, as shown in Fig. 8. This is consistent with estimates based on measured dust content and composition in South Pole ice. It must be kept in mind, however, that the exponential fit to the intrinsic absorption coefficient is only a phenomenological procedure. To the statistical error bars in Fig. 8 must therefore be added a systematic uncertainty of unknown magnitude.

We note that our results at 830-m depth give values for the absorption coefficient that represent the purest ice ever measured. Because a residual dust component is known to exist also at these depths, the results for $\alpha_{\mathrm{abs}}$ must be interpreted as upper bounds for the intrinsic absorption coefficient of pure ice.

For completeness, in Appendix A we give a brief description of scattering on dust grains, expected to be the dominant contribution to the turbidity at larger, bubble-free depths.

### C. Three-Component Model of Absorption in Dusty Ice

To summarize the results of this section, Fig. 9 shows a three-component model that we expect to apply to absorption by ice with an extremely low content of

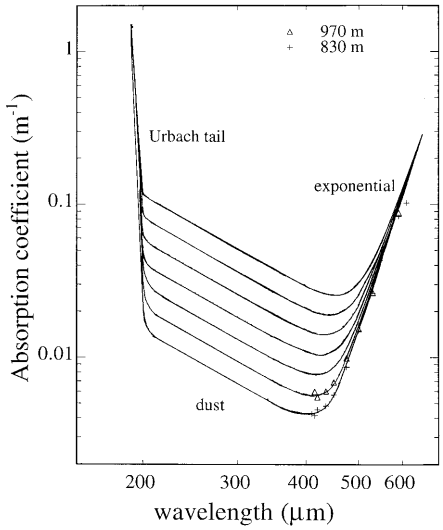


Fig. 9. Three-component model of absorption by ice containing insoluble dust but no dissolved impurities. The concentrations of dust increase by factors of 1.4 for each curve.

dissolved impurities. Component 1, which dominates in the ultraviolet, is the exponential Urbach tail, given by

$$\alpha_{UV} = A_{UV} \exp(-0.4818\lambda), \tag{44}$$

where $A_{UV}$ is proportional to the density of insoluble dust in ice. As with ionic solids, the slope of the Urbach tail may show a weak dependence on measurement temperature.

Component 2, which dominates in the near UV and blue, is the contribution of insoluble dust, which we assume to have a size distribution similar to that of the aerosols studied by Lindberg and Laude.[24] Fitting their absorption data to a power law in the region $300 \le \lambda \le 700$ nm leads to a dependence proportional to $\lambda^{-2}$ for measurements made both in 1974 and in 1994. We assume the same $\lambda^{-2}$ dependence for dust in South Pole ice:

$$\alpha_{dust} = A_{dust}\lambda^{-2}. \tag{45}$$

Component 3 is the exponential rise in the red and infrared, as parametrized in Eq. (42).

From Subsection 4.B, we take $A_{dust}$ at a depth of 970 m to be 1.4 times that at 830 m. The family of curves in Fig. 9 is for values of $A_{dust}$ increasing incrementally by factors of 1.4.

None of the curves in Fig. 9 fits the data for laboratory ice, nor should they. As we noted above, the contribution of scattering was not distinguished from absorption in those experiments.[6–8] Even if scattering had been excluded, the laboratory ice had been made from not very pure water and thus probably contained dissolved impurities that contributed their own absorption bands to the ice.

## 5. Discussion and Conclusions

The pulsed laser method, applied by way of optical fiber to deep ice, provides a highly successful method of independently measuring absorption and scattering as a function of wavelength over the interval 400–650 nm.

Previous laboratory studies of absorption of ice at visible and near-visible wavelengths where the scattering length is comparable to or less than the absorption length are probably in error because of failure to determine the two parameters separately and probably also to a greater concentration of impurities in ice made from laboratory water than in Antarctic ice. Our research has shown that the intrinsic absorption of pure ice decreases to values less than a few times $10^{-3}$ m$^{-1}$ at wavelengths between 300 and 400 nm. Our pulsed laser results support the conjecture that the absorption increases exponentially with wavelength in the red region. We believe it would be worthwhile for quantum chemists to seek a theoretical basis for the exponential behavior.

The optical measurements by the AMANDA collaboration, initially intended for calibration purposes, have revealed surprising properties of pure ice. The remarkably low intrinsic absorption in the visible and near-UV region may lead to interesting applications for physics and astrophysics. Our simple three-component model for absorption by pure but dust-bearing ice (Fig. 9) will be subjected to a critical test when the data at depths 1500–1900 m taken in 1996 become available. In those experiments we will measure absorption and scattering at wavelengths of 337, 350, and 380 nm as well as in the region 410 to 650 nm.

## Appendix A. Simulations of Scattering on Dust Grains in Antarctic Ice

Although we have reasons to believe that the optical properties of Antarctic ice will be dramatically better at depths where the air bubbles have transformed into clathrates, for future use we want to estimate the residual scattering on ice crystal boundaries, clathrates, dust, and other impurities, as well as Rayleigh scattering in the ice itself.

It is only dust (including soot) of these sources that contributes measurably to absorption. We first briefly discuss the scattering properties of dust, given the absorption coefficients derived in Section 4.

The total concentration of insoluble impurities in recently deposited South Pole ice has been estimated to be around 15 ng/g.[25] The size distribution of dust grains has also been measured[26,27] at the South Pole. At another Antarctic location (Dome C), deep samples have been taken and analyzed with a scanning electron microscope (giving the number versus radius distribution), a Coulter counter (giving the volume distribution), and laser nephelometry (giving the combined scattering function of a melted ice sample).[23] In the latter work, the data could be well fitted by a log normal distribution with a modal radius of 0.25 μm (for the number-to-log radius size distribution). Using this size distribution and applying Mie-scattering theory, they could get satisfactory agreement with the measured scattering function, except at large angles where perhaps effects of the nonspherical shapes of dust grains appear.

We developed Mie-scattering programs to verify the findings of Royer *et al*. for the scattering function. However, when simulations for a large detector such as AMANDA have to be done, it is useful to find approximations that give results much faster than CPU time-consuming Mie calculations on an event-by-event basis.

We found that a surprisingly good approximation to the results in Ref. 23 can be obtained by simply using first-order geometrical optics (neglecting internal reflections) on dust grains, i.e., by just calculating the deviation angle according to Snell's law. This is only a function of where on the beam-facing surface of the sphere the light ray enters. We generate a radial variable $r$ at random by setting $r = \sqrt{x}$ ($x$ is a random number distributed between 0 and 1, and the square root makes the geometric weight for a given $r$ proportional to $r$). The scattering angle for the Monte-Carlo simulation can simply be taken as

$$\delta\theta = 2[\arcsin(r) - \arcsin(r/n_{rel})], \tag{A1}$$

where $n_{\mathrm{rel}}$ is the relative refraction index ($\sim$1.18) between dust and ice.

The expression (A1) has the drawback that it underestimates large-angle scattering somewhat. In contrast to the multiple-scattering case on air bubbles discussed above, where only $\tau = \langle \cos\theta \rangle$ is of importance, for reasonable possible spacings between PMT's in a working detector only a few scatterings on dust will occur and therefore the full scattering function is more important. We have thus chosen a strategy that is based on the Henyey–Greenstein approximation to the scattering function:

$$\frac{d\sigma}{d(\cos\theta)} = \frac{1-\tau^2}{(1+\tau^2-2\tau\cos\theta)^{3/2}}. \tag{A2}$$

This accurately reproduces the true scattering function once the value of $\tau = \langle \cos\theta \rangle$ is known. To find the latter, we calculated it using Mie theory, with the known properties of the dust in South Pole ice as input. For the values of Dome C,[23] we find $\tau \approx 0.92$. For use in a simulation program, Eq. (A2) must be integrated and inverted. Setting now $r = x$ ($x$: random number uniformly distributed between 0 and 1), we find that a distribution of the form is obtained by choosing

$$\cos\theta = \frac{2r(1-\tau+r\tau)(1+\tau)^2}{(1-\tau+2r\tau)^2} - 1. \tag{A3}$$

The $1 + \cos^2\theta$ distribution applicable to Rayleigh scattering is similarly generated by our choosing

$$\cos\theta = 2\left(\kappa^{1/3} - \frac{1}{4}\kappa^{-1/3} + \frac{1}{2}\right) - 1, \tag{A4}$$

where

$$\kappa = -\frac{1}{4} + \frac{1}{2}r + \frac{1}{8}\sqrt{5 - 16r + 16r^2}. \tag{A5}$$

There is a difference between the measured dust size distributions at Dome C and at the South Pole. In the latter case, the modal radius is around 0.1 $\mu$m (compared with 0.25 at Dome C). This makes the scattering distributions markedly wider as a consequence of the approach to the Rayleigh-scattering regime, which is isotropic on the average.

It is customary to define the albedo $\omega$ as the ratio of scattering to extinction (i.e., scattering plus absorption) cross sections. The absorption in dust depends on the imaginary part of the refractive index, which has been measured to be typically between $-0.003$ and $-0.007$ for atmospheric dust.[28] From the Mie computations (using again a log normal size distribution) we obtain values of the albedo between 0.9 and 0.96, both at 500 and 350 nm, when the real part of the refractive index of dust varies between 1.53 and 1.56 and the imaginary part between $-0.003$ and $-0.007$. This is not too different from the values inferred from the Dome C data in Ref. 23. The values of $\tau = \langle \cos\theta \rangle$ are, however, much smaller: $\sim$0.70 for 500 nm and $\sim$0.74 for 350 nm (not much dependent on the value of the imaginary index). The results using a so-called Junge law distribution $dn/d(\log r) \propto r^c$, with $c \sim -1.9$ are similar, except that the albedo depends more strongly on the imaginary part of the refractive index. This seems to be due to the effects of Mie-type resonances whose exact location in size parameter depends on both the real and imaginary parts of the index. The values of the effective scattering power [defined analogously to Eq. (15)] are relatively stable and correspond to $\omega$ and $\tau$ both being around 0.8–0.9.

We note that typical scattering lengths on dust grains in the 800–1000-m depth range are expected to be of the order of 50 m. Therefore scattering on air bubbles dominates completely. For greater depths, however, the results of this Appendix should be of use.

We are grateful to Y. He and A. Westphal for useful comments on the manuscript. L. Bergström acknowledges support from the Swedish Natural Science Research Council and the Stockholm University–University of California, Berkeley exchange program. P. B. Price acknowledges support under the National Science Foundation grant PHY-9307420 and the Uppsala University–University of California, Berkeley exchange program. The AMANDA collaboration is indebted to the Polar Ice Coring Office and to Bruce Koci for the successful drilling operations, and to the National Science Foundation, the Swedish Natural Science Research Council, the K. A. Wallenberg Foundation, the Swedish Polar Research Secretariat, and the German Electron Synchrotron Institute DESY for their support.

### References and Note

1. P. C. Mock, P. Askebjer, S. W. Barwick, L. Bergström, A. Bouchta, S. Carius, B. Erlandsson, A. Goobar, L. Gray, A. Hallgren, F. Halzen, H. Heukenkamp, P. O. Hulth, J. Jacobsen, S. Johansson, V. Kandhadai, A. Karle, I. Liubarsky, D. M. Lowder, T. C. Miller, R. Morse, R. Porrata, P. B. Price, A. Richards, H. Rubinstein, Ch. Spiering, Q. Sun, Th. Thon, S. Tilav, C. Walck, R. Wischnewski, and G. Yodh, "Status and capabilities of AMANDA-94," in *Proceedings of the 24th International Cosmic Ray Conference* (Istituto Nazionale di Fisica Nucleare, Rome, 1995), pp. 758–761; L. Gray, P. Askebjer, S. W. Barwick, L. Bergström, A. Bouchta, S. Carius, B. Erlandsson, A. Goobar, A. Hallgren, F. Halzen, H. Heukenkamp, P. O. Hulth, J. Jacobsen, S. Johansson, V. Kandhadai, A. Karle, I. Liubarsky, D. M. Lowder, T. C. Miller, P. C. Mock, R. Morse, R. Porrata, P. B. Price, A. Richards, H. Rubinstein, Ch. Spiering, Q. Sun, T. Thon, S. Tilav, C. Walck, R. Wischnewski, and G. Yodh, "The design of a neutrino telescope using natural deep ice as a particle detector," in *Proceedings of the 24th International Cosmic Ray Conference* (Istituto Nazionale di Fisica Nucleare, Rome, 1995), pp. 816–819; S. Tilav, "Indirect evidence for long absorption lengths in Antarctic ice," in *Proceedings of the 24th International Cosmic Ray Conference* (Istituto Nazionale di Fisica Nucleare, Rome, 1995), pp. 1011–1014.
2. P. Askebjer, S. W. Barwick, L. Bergström, A. Bouchta, S. Carius, A. Coulthard, K. Engel, B. Erlandsson, A. Goobar, L. Gray, A. Hallgren, F. Halzen, P. O. Hulth, J. Jacobsen, S. Jahansson, V. Kandhadai, I. Liubarsky, D. Lowder, T. Miller, P. C. Mock, R. Morse, R. Porrata, P. B. Price, A. Richards, H. Rubinstein, E. Schneider, Q. Sun, S. Tilav, Ch. Walck, and G. Yodh, "Optical properties of the South Pole ice at depths between 0.8 and 1 kilometer," Science **267,** 1147–1150 (1995).

3. P. Askebjer, S. W. Barwick, L. Bergström, A. Bouchta, S. Carius, B. Erlandsson, A. Goobar, L. Gray, A. Hallgren, F. Halzen, H. Heukenkamp, P. O. Hulth, J. Jacobsen, S. Johansson, V. Kandhadai, A. Karle, I. Liubarsky, D. M. Lowder, T. C. Miller, P. C. Mock, R. Morse, R. Porrata, P. B. Price, A. Richards, H. Rubinstein, Ch. Spiering, Q. Sun, Th. Thon, S. Tilav, Ch. Walck, R. Wischnewski, and G. Yodh, "Wavelength Dependence of Light Scattering and Absorption in Deep Glacier Ice," Geophys. Res. Lett. (1997).
4. T. Uchida, W. Shimada, T. Hondoh, S. Mae, and N. I. Barkov, "Refractive-index measurements of natural air-hydrate crystals in an Antarctica ice sheet," Appl. Opt. **34,** 5746–5749 (1995).
5. P. B. Price and L. Bergström, "Optical properties of deep ice at the South Pole: scattering," Appl. Opt. **36,** 000–000 (1997). Ao 011889
6. T. C. Grenfell and D. K. Perovich, "Radiation absorption coefficients of polycrystalline ice from 400–1400 nm," J. Geophys. Res. **86,** 7447–7450 (1981).
7. D. K. Perovich and J. W. Govoni, "Absorption coefficients of ice from 250 to 400 nm," Geophys. Res. Lett. **18,** 1233–1235 (1991).
8. S. G. Warren, "Optical constants of ice from the ultraviolet to the microwave," Appl. Opt. **23,** 1206–1225 (1984).
9. M. S. Patterson, B. Chance, and B. C. Wilson, "Time resolved reflectance and transmittance for the non-invasive measurements of tissue optical properties," Appl. Opt. **28,** 2331–2336 (1989); A. Ishimaru, "Diffusion of a pulse in densely distributed scatterers," J. Opt. Soc. Am. **68,** 1045–1050 (1978).
10. S. Chandrasekhar, "Stochastic problems in physics and astronomy," Rev. Mod. Phys. **15,** 1–88 (1943).
11. H. Miller, "Physical properties of ice," in Vol. 1b of *Landolt-Börnstein Numerical Data and Functional Relationships in Science and Technology*, K.-H. Hellwege, ed. (Springer-Verlag, New York, 1982), pp. 494–507.
12. W. C. Davidon, "Variance algorithm for minimization," Comput. J. **10,** 406–410 (1968).
13. T. I. Quickenden and J. A. Irvin, "The ultraviolet absorption spectrum of liquid water," J. Chem. Phys. **72,** 4416–4428 (1980).
14. T. Tomiki and T. Miyata, "Optical studies of alkali fluorides and alkaline earth fluorides in VUV region," J. Phys. Soc. Jpn. **27,** 658–678 (1969); E. D. Palik and W. R. Hunter, "Lithium fluoride," in *Handbook of Optical Constants of Solids*, E. D. Palik, ed. (Academic, New York, 1985), pp. 675–693.
15. T. C. McGill, "Theory of multiphoton absorption: a review," in *Optical Properties of Highly Transparent Solids*, S. S. Mitra and B. Bendow, eds. (Plenum, New York, 1975), p. 3.
16. I. A. Belolaptikov, L. B. Bezrukov, B. A. Korisovets, E. V. Bugaev, G. V. Domogatskii, L. A. Donskich, A. A. Doroshenko, Zh. A. M. Dzhilkibaev, M. D. Galperin, M. N. Gushtan, A. M. Klabukov, S. I. Klimushin, O. Dzh. Lanin, B. K. Lubsandorzhev, N. V. Ogievetskii, A. I. Panfilov, I. A. Sokalski, I. I. Trofimenko, N. M. Budnev, A. G. Chenskii, V. I. Dobrynin, O. A. Gress, A. P. Koshechkin, Dzh. B. Lanin, G. A. Litunenko, A. V. Lopin, V. A. Naumov, M. I. Nemchenko, Yu. A. Parfenov, A. A. Pavlov, O. P. Pokalev, V. A. Primin, A. A. Sumanov, V. A. Tarashanskii, V. L. Zurbanov, A. V. Golikov, E. S. Zaslavskaya, V. B. Kabikov, L. A. Kuzmichov, E. A. Osipova, G. N. Dudkin, V. Yu. Egorov, A. A. Lukanin, A. M. Ovcharov, V. M. Padalko, A. H. Padusenko, S. D. Alatin, S. V. Fialkovskii, V. F. Kulepov, M. B. Milenin, A. A. Levin, A. I. Nikiforov, M. I. Rosanov, H. Heukenkamp, J. Krabi, T. Mikolajski, C. Spiering, R. Wischnewski, L. Jenek, D. Kiss, L. Tanko, Yu. S. Kusner, V. A. Poleshchuk, and P. P. Sherstyankin, "The Lake Baikal deep underwater detector," in Nucl. Phys. B (Proc. supp.) **19B,** 388–395 (1991).
17. J. Babson, B. Barish, R. Becker-Szendy, H. Bradner, R. Cady, J. Clem, S. T. Dye, J. Gaidos, P. Gorham, P. K. F. Grieder, T. Kitamura, W. Kropp, J. G. Learned, S. Matsuno, R. March, K. Mitsuni, D. O'Connor, Y. Oshashi, A. Okada, V. Peterson, L. Price, F. Reines, A. Roberts, C. Roos, H. Sobel, V. J. Stenger, M. Webster, and C. Wilson, "Cosmic-ray muons in the deep ocean," Phys. Rev. D **42,** 3613–3620 (1990).
18. R. C. Smith and K. S. Baker, "Optical properties of the clearest natural waters," Appl. Opt. **20,** 177–184 (1981).
19. S. Noël and H. Mes, "The measurement of the attenuation of light by water in SNO," SNO preprint STR-91-062, Sudbury Neutrino Observatory, Canada (personal communication, 1991).
20. I. A. Belolaptikov, L. B. Bezrukov, B. A. Borisovets, N. M. Budnev, A. G. Chenskii, I. A. Danilchenko, Zh. A. M. Dzhilkibaev, V. I. Dobrynin, G. V. Domogatskii, L. A. Donskich, A. A. Doroshenko, S. V. Fialkovskii, A. A. Garus, O. A. Gress, T. A. Gress, H. Heukenkamp, A. Karle, A. M. Klabukov, A. I. Klimov, S. I. Klimushin, A. P. Koshechkin, J. Krabi, V. F. Kulepov, L. A. Kuzmichov, B. K. Lubsandorzhev, M. B. Milenin, T. Mikolajski, R. R. Mirgazov, N. L. Moseiko, S. A. Nikiforov, E. A. Osipova, A. I. Panfilov, Yu. V. Parfenov, A. A. Pavlov, D. P. Petukhov, K. A. Pocheikin, P. G. Pokhil, P. A. Pokalev, M. I. Rosanov, V. Yu. Rubzov, S. I. Sinegovskii, I. A. Sokalski, C. Spiering, O. Streicher, V. A. Tarashanskii, T. Thon, L. I. Trofimenko, C. Wiebusch, and R. Wischnewski, "Variation of water parameters at the site of the Baikal experiment and their effect on the detector performance," in *Proceedings of the 24th International Cosmic Ray Conference*, (Istituto Nazionale di Fisica Nucleare, Rome, 1995), pp. 770–772.
21. P. B. Price, P. Askebjer, S. W. Barwick, L. Bergström, A. Bouchta, S. Carius, B. Erlandsson, A. Goobar, L. Gray, A. Hallgren, F. Halzen, H. Heukenkamp, P. O. Hulth, J. Jacobsen, S. Johansson, V. Kandhadai, A. Karle, I. Liubarsky, D. M. Lowder, T. C. Miller, P. C. Mock, R. Morse, R. Porrata, A. Richards, H. Rubinstein, Ch. Spiering, Q. Sun, S. Tilav, T. Thon, C. Walck, R. Wischnewski, A. J. Westphal, and G. Yodh, "Optical properties of South Pole ice for neutrino astrophysics," in *Proceedings of the 24th International Cosmic Ray Conference*, (Istituto Nazionale di Fisica Nucleare, Rome, 1995), pp. 777–780.
22. AMANDA Collaboration, "On the age *vs* depth and optical clarity of deep ice at South Pole," J. Glaciol. **41,** 445–454 (1995).
23. A. Royer, M. De Angelis, and J. R. Petit, "A 30000 year record of physical and optical properties of microparticles from an east Antarctic ice core and implications for paleoclimate reconstruction models," Climatic Change **5,** 381–412 (1983). Royer *et al*. inferred from the optical scattering properties of melted ice core samples from Dome C that the particle size distribution and complex refractive index of dust show no depth dependence, although it is not clear to us that these conclusions were strongly supported by their data.
24. J. D. Lindberg and L. S. Laude, "Measurement of the absorption coefficient of atmospheric dust," Appl. Opt. **13,** 1923–1927 (1974); J. D. Lindberg, "Absorption-coefficient-determination method for particulate materials," Appl. Opt. **33,** 4314–4319 (1994).
25. M. Kumai, "Identification of nuclei and concentrations of chemical species in snow crystals sampled at the South Pole," J. Atmos. Sci. **33,** 833–841 (1976); R. Delmas, M. Briat, and M. Legrand, "Chemistry of South Pole snow," J. Geophys. Res. **87,** 4314–4318 (1982).
26. R. I. Gayley and M. Ram, "Atmospheric dust in polar ice and the background aerosol," J. Geophys. Res. **90,** 12921–12925 (1985).
27. E. Mosley-Thompson, Byrd Polar Research Center and Department of Geography, Ohio State University, Columbus, Ohio 43210 (personal communication, 1995).
28. G. A. d'Almeida, P. Koepke, and E. P. Shettle, *Atmospheric Aerosols—Global Climatology and Radiative Characteristics* (Deepak, Hampton, Va., 1991).